International Journal of Solids and Structures 50 (2013) 623–636

Contents lists available at SciVerse ScienceDirect

International Journal of Solids and Structures

journal homepage: www.elsevier.com/locate/ijsolstr

Simulation of ship grounding damage using the finite element method

Anuar AbuBakar [a], R.S. Dow [b,*]

[a] Department of Maritime Technology, University Malaysia Terengganu, Malaysia
[b] School of Marine Science and Technology, Newcastle University, England, UK

ARTICLE INFO

Article history:
Received 30 June 2011
Received in revised form 19 June 2012
Available online 2 November 2012

Keywords:
Progressive failure
Plastic deformation
Rupture
Finite element analysis (FEA)
Ship grounding damage

ABSTRACT

This paper presents a comparison with experimental data of the resistance of stiffened panels to penetration damage. It also carried out comparisons between numerical simulations and experiments investigating the grounding of ships. The finite element method and FEA software are used to predict penetration damage and this modelling simulation is then extended to investigate damage to a ship's double bottom structure in different grounding scenarios. The progressive failure of the double bottom is investigated in terms of plastic deformation and also the evolution of damage including material rupture. Three different levels of complexity were used in modelling the double bottom structure concerning the inner and outer shell plating; longitudinal stiffeners in the shell plating, and structures with stiffening in longitudinal floors. The analysis was carried out in the ABAQUS explicit code.

The results presented include the crushing force as a function of time, an investigation of the energies involved in the plastic deformation and rupture of the double bottom structure, and comparisons with experimental data where available.

1. Introduction

In the past, most studies of collisions and grounding were carried out using a combination of mathematical and experimental approaches. Since the late 1990s (Kitamura, 2002) the rapid progress of computer technology has made large-scale finite element analysis (FEA) practicable, while further progress in analytical methods has been relatively slow. In order to meet the increasing demands from the shipbuilding industry for reliability and cost-efficiency, FEM approaches are new applied more often in the direct quantitative estimation of crashworthiness and also for the validation and verification of simplified analytical methods.

Previous studies have used either theoretical, experimental on numerical approaches. Currently there are a range of different approaches and codes available on the market that are capable of predicting damage to ship structures during grounding. These approaches include damage modelling, such as the Forming Limit Diagram (FLD) (Keeler and Backofen, 1963; Jie et al., 2009), The Rice–Tracey and Cockcroft–Latham (RTCL) model (Alsos and Amdahl, 2007; Alsos et al., 2009), The Bressan, Williams and Hill (BWH) model (Alsos et al., 2008, 2009) as well as other approaches. In this analysis the forming limit diagram method was used as a model of material failure for dynamic loading using the properties described below.

The present analysis was divided into two parts. Firstly the penetration of a double bottom structure and grounding comparison with numerical and experimental results (Rodd, 1996; Alsos et al., 2008, 2009; Alsos and Amdahl, 2009). Secondly the analysis was extended to a typical double bottom application using the same material failure model and looking at vertical penetration followed by longitudinal movement along the compartment.

2. Material characterisation

2.1. Material model

The material is assumed to be isotropic and to exhibit strain hardening properties as described by Ludwik's strain hardening power law:

$$\sigma = K\varepsilon^n \tag{1}$$

To describe the time dependence of the material response, the following true stress-natural strain relation was employed using deformation theory, here K, m and n are material parameters, and m lies between 0 and 0.05 (Hutchinson and Neale, 1978).

$$\sigma = K\varepsilon^n\dot{\varepsilon}^m \tag{2}$$

Hence, the true stress–strain relation is approximated by Eq. (3) below assuming isotropic material properties, where ε_{plat} is the plateau strain proposed by (Alsos et al., 2009).

* Corresponding author. Tel.: +44 0 7834241856.
E-mail addresses: anuarbakar@umt.edu.my (A. AbuBakar), r.s.dow@newcastle.ac.uk, anuarbakar@umt.edu (R.S. Dow).

0020-7683/$ - see front matter © 2012 Elsevier Ltd. All rights reserved.
http://dx.doi.org/10.1016/j.ijsolstr.2012.10.016

$$\sigma = \begin{cases} \sigma_y & \text{if} \quad \varepsilon \leqslant \varepsilon_{plat} \\ K(\varepsilon + \varepsilon_0)^n \dot{\varepsilon}^m & \text{otherwise} \end{cases} \tag{3}$$

and

$$\varepsilon_0 = \left(\frac{\sigma_y}{K}\right)^{1/n} - \varepsilon_{\text{plat}}. \tag{4}$$

here a quasi-linear stress–strain relationship (Jie et al., 2009) can be approximately written as:

$$\dot{\varepsilon} = \left[\frac{\varepsilon}{(m+n)} - s(\sigma,\varepsilon)\right]\frac{\dot{\sigma}}{\sigma} + \left(\frac{\sigma}{K\varepsilon^n}\right)^{1/m} \tag{5}$$

here

$$s(\sigma,\varepsilon) = \frac{-c\sigma}{\varepsilon^{n/m}} \tag{6}$$

and

$$\dot{\sigma} = E_t\dot{\varepsilon}. \tag{7}$$

Here, E_t is tangent modulus for plastic deformation and C is an integration constant, which can be determined from uniaxial testing at various strain rates.

In cases where the collision and grounding event occurs at relatively low speeds, the strain rate effect described in Eq. (3) is usually ignored. This was the procedure applied in the analysis carried out in this study, which means that the equation is reduced to that proposed by (Hill, 1991).

2.2. Material failure

The material model applied in Section 2.1 models the plastic deformation of the structure during collision and grounding events. This has to be coupled with a material failure model in order to predict the onset of rupture. In this work the authors have adopted the Forming Limit Diagram (FLD) approach to predict the onset of rupture.

The Forming Limit Diagram (FLD) method for predicting material failure was introduced by (Keeler and Backofen, 1963) to determine the amount of deformation that a material can withstand prior to the onset of necking instability. The maximum strains that a sheet material can sustain prior to the onset of necking are referred to as the forming limit strains.

When considering the forming limit strains including rate-dependant effects in FLD (details of which can be found in (Jie et al., 2009), the following relationships are used;

$$\varepsilon_1 = \begin{cases} \frac{(m+n)}{1+r_\varepsilon} + \frac{\sqrt{3}(m+n)s(\sigma_{eq}\varepsilon_{eq})}{\sqrt[2]{1+r_\varepsilon+r_\varepsilon^2}} & \text{if} \quad r_\varepsilon \leqslant 0 \\ \frac{3r_\varepsilon^2+(m+n)(2+r_\varepsilon)^2}{2(2+r_\varepsilon)(1+r_\varepsilon+r_\varepsilon^2)} + \left(\frac{(m+n)3(\sigma_{eq}\varepsilon_{eq})}{2(2+r_\varepsilon)(1+r_\varepsilon+r_\varepsilon^2)}\right)[(2+r_\varepsilon)\sqrt{3(1+r_\varepsilon+r_\varepsilon^2)}\varepsilon_{eq} - 3r_\varepsilon^2] & \text{if} \quad r_\varepsilon > 0 \end{cases} \tag{8}$$

here ε_{eq} is the equivalent strain which, for the Von Misses, criterion defined as;

$$\varepsilon_{eq} = \frac{2}{\sqrt{3}}\varepsilon_1\sqrt{1+r_\varepsilon+r_\varepsilon^2} \tag{9}$$

.where: $r_\varepsilon = \frac{\varepsilon_2}{\varepsilon_1}$ is the strain ratio ($r_\varepsilon = 0$ for plain strain, $r_\varepsilon = -0.5$ for simple tension and $r_\varepsilon = 1$ for biaxial tension) which is the basis for localised necking failure.

This FLD material failure has been compared with experimental results using the RCTL and BWH failure models in predicting the resistance of stiffened panels to penetration damage.

The RCTL damage criterion is a combination of the modified Rice Tracey and Cockcroft–Latham damage criterion. Both of these functions are based on the hydrostatic stress state, express by the stress triaxiality: $T = \frac{\sigma_m}{\sigma_{eq}}$, where σ_m is hydrostatic stress and σ_{eq} is the equivalent stress.

The value of T lies between $-1/3 < T < 1/3$ and damage ceases when $T < -1/3$, which is referred to as the cut-off value below which fracture will not occur.

The BWH criterion is based on the onset of local necking as a failure mechanism. The model describes an analytical forming limit curve in stress space and is employed by several authors as follow:

$$\sigma_1 = \begin{cases} \frac{2K}{\sqrt{3}}\frac{1+\frac{1}{2}r_\varepsilon}{\sqrt{r_\varepsilon^2+r_\varepsilon+1}}\left(\frac{2}{\sqrt{3}}\frac{n}{1+r_\varepsilon}\sqrt{r_\varepsilon^2+r_\varepsilon+1}\right)^n & \text{if} \quad r_\varepsilon \leq 0 \\ \frac{2K}{\sqrt{3}}\frac{\left(\frac{2}{\sqrt{3}}n\right)^n}{\sqrt{1-\left(\frac{r}{2+r_\varepsilon}\right)^2}} & \text{otherwise} \end{cases} \tag{10}$$

Both of these failure models are described in detail in (Alsos et al., 2008; Alsos et al., 2009).

2.3. Material properties

The Materials used in this analysis were mild steel (S235JR-EN10025) and high strength steel (S355NH-EN10210), the material properties are describe in Table 1. The properties in this table were obtained experimentally.

3. Finite element modelling

3.1. The element characteristic length

Finite element analysis is a technique which gives approximate solutions, and its accuracy depends on a number of factors which include mesh density. When considering material failure such as rupture, where the material will exhibit strain-softening and necking characteristics, mesh density can be an important factor in the prediction of failure.

The damage evolution model included in the ABAQUS programme allows the analyst to compensate for the strain softening effect that occurs in the material between necking and rupture. In the context of an elastic–plastic material with isotropic hardening, the damage manifests itself in two forms: an effective reduction of the material yield stress coupled with a degradation of material stiffness. Fig. 1 represents the damaged stress–strain response, while the dashed curve is the response in the absence of damage. (i.e. the true stress–strain curve.).

Material failure is normally expressed in terms of stress–strain relationships, as shown in Fig. 1(a) and (b). During loading the material will undergo damage processes which follow a la of evolution where damage starts to initiate at point $D = 0$ and full degradation occurs when D reaches a maximum where $D_{\max} \leqslant 1$. The equivalent plastic stress and strain at the onset of necking are denoted by σ_{y0}, $\bar{\varepsilon}_0^{pl}$ respectively, where $\bar{\sigma}$ is the true stress curve in the absence of damage or a fully plastic condition and σ_0 is the yield stress. Finally, elements which fail are removed from the model when they satisfy the maximum damage evolution law as $D_{\max} \leqslant 1$.

The evolution of the damage variable with relative plastic displacement can be specified in tabular, linear, or exponential forms. Instantaneous failure will occur if the plastic displacement at failure u_f^{pl}, is specified as 0; however, this choice is not recommended and should be used with care because it causes a sudden drop in stress at the ultimate strength of material point that can lead to dynamic instabilities.

Throughout this study a linear softening law was adopted for simplicity. The value of strain for the onset of damage is estimated as being $0.5\varepsilon_f$. This is a typical value which reflects the ultimate strength of steel before softening starts to take place. The softening

Table 1
The properties of steel taken from (Alsos and Amdahl, 2009; Alsos et al., 2009) and were obtained experimentally.

Material type	Material grade	K (MPa)	n	ε_{plate}	ε_f	σ_y (MPa)	σ_u (MPa)
A	S235JR-EN10025	740	0.24	–	0.35	285	416
B	S235JR-EN10025	760	0.225	0.015	0.35	340	442
C	S255JR-EN10210	830	0.18	0.01	0.28	390	495

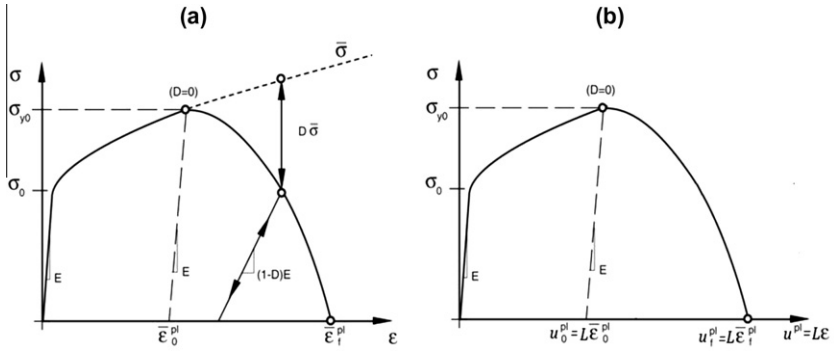

Fig. 1. (a) ABAQUS documentation stress-strain curve with progressive damage degradation. (b) Stress–strain curve with progressive damage degradation dependent on mesh density (Yu and Jeong 2010).

or evolution of the damage is controlled by the gradient of material damage, where 0 is the sudden deletion of an element after the FLD failure criterion is satisfied and 1 denotes fully plastic behaviour (with no deletion of elements). The softening of the material will occur when the damage criteria is applied to initiate the local necking before rupture. For the purposes of this study the engineering fracture strains listed in Table 1 have been adopted, at $\varepsilon_f = 0.35$ and 0.28 for mild steel and high tensile steel respectively.

Additional analyses were run with larger values of rupture strain in the true stress/strain relationship modelled in ABAQUS. The results for this value demonstrated little effect on the local necking and fracture behaviour observed in the analysis.

The literature reviewed comes to no real conclusion about the characteristic element length required for solution accuracy; hence the need for mesh convergence studies see, for example, (Wiśniewski and Kołakowski, 2003; Zhang and Suzuki, 2005; Alsos et al., 2009). Abaqus Explicit tries to resolve the problem by introducing an element characteristic length which is related to element size.

Fig. 1(b) shows the damage evolution law embedded with mesh dependency where u^{pl} is the fracture work conjugate of the yield stress after the onset of damage (work per unit area of the crack), u_0^{pl} is the damage initiation point u_f^{pl} represent fully degraded material where the elements will be removed from the model, and L is the mesh element characteristic length. For shell and 2D elements, L is the square root of the integration area and for 3D elements, it is the integration of volume, where $\bar{\varepsilon}_f^{pl}$ is determined from uniaxial tension tests and assumed to be the same as ε_f in Table 1.

3.2. Finite element procedure

The FE analysis was performed in Abaqus explicit using S4R shell elements with general surface contact. Thickness integration was carried out using the Simpson rule with 5 integrations points through the thickness.

The modelling of the materials plastic behaviour was carried out using a power law expression as discussed above in Section 2.1. The relationship between fracture strain and element size is discussed by various authors (Alsos et al., 2009; Ehlers, 2009) using a scaling law applied to Eq. (3). This neglects the effect of strain rate, where the true stress strain curve is modified according to mesh size. (Lehmann and Peschmann, 2002) also use the same method where the material properties are modified using the scaling law and the critical fracture strain is calculated for different mesh sizes.

For the purposes of this study, material properties were generated using Eq. (3) and adopting the values listed in Table 1. A mesh convergence study was then carried out and is discussed next. The input parameter defining the onset necking using the FLD damage criterion is calculated using Eq. (11). The hardening numbers are adopted from Table 1 as 0.24, 0.225 and 0.18 for material types A, B and C respectively.

4. On the resistance of stiffened panels to penetration damage

A series of experimental tests were carried out by (Alsos and Amdahl, 2009) under quasi-static conditions, which were compared with previous FEA simulations (Alsos et al., 2009) using both RTCL and BWH damage evolution criteria. Their results are shown below in Fig. 4(a)–(c) alongside those of the present FEA analysis using the FLD damage failure model. The current FEA simulations use of an element mesh size 15 mm and only require simple damage input parameters. However the results produced are consistent and reliable when compared to the actual experimental results.

The FEA analysis conducted ignored the strain rate effect, where $m = 0$ and $s = 0$ in Eq. (8). Then the FLD failure model as expressed in Eq. (8) becomes:

$$\varepsilon_1 = \begin{cases} \frac{n}{(1+r_\varepsilon)} & \text{if } r_\varepsilon \leqslant 0 \\ \frac{3r_\varepsilon^2+(2+r_\varepsilon)^2 n}{2(2+r_\varepsilon)(1+r_\varepsilon+r_\varepsilon^2)} & \text{if } r_\varepsilon > 0 \end{cases} \tag{11}$$

4.1. Stiffened panel analysis

The panels identified were manufactured and tested by (Alsos and Amdahl, 2009) in order to provide a simulation and analysis of the grounding scenario (see Fig. 2(a)–(c)). The tests were carried out by laterally forcing an "indenter" to a depth of about 0.25 m, as shown in Fig. 3(d), into the centre of a plate of the size of 720 × 1200 × 5 mm made form material Type A from Table 1.

The configurations of the structure are as follows:

a. Penetration of flat panel
b. Penetration on stiffener of single stiffened panel
c. Penetration of stiffened panel between two stiffeners.

For the stiffened panel cases, the plate stiffeners (120 × 6 mm flat bars) were made from material Type B from Table 1 and were evenly spaced as shown in Fig. 2(b) and (c). The 300 × 200 × 12.5 mm hollow square frame supporting the test panels was assumed to be fully fixed as shown in Fig. 3(a). Fig. 2(d) shows the penetration of the "indenter" in the experiment taken from (Alsos and Amdahl, 2009). Both the experiment and numerical simulations were carried out under quasi-static conditions.

4.2. Mesh convergence studies

Mesh convergence studies were conducted in order to find the most suitable mesh for using in grounding damage studies for both stiffened panels and double bottom structures. The mesh chosen is always a compromise between the accuracy, computer resources and reasonable computational time.

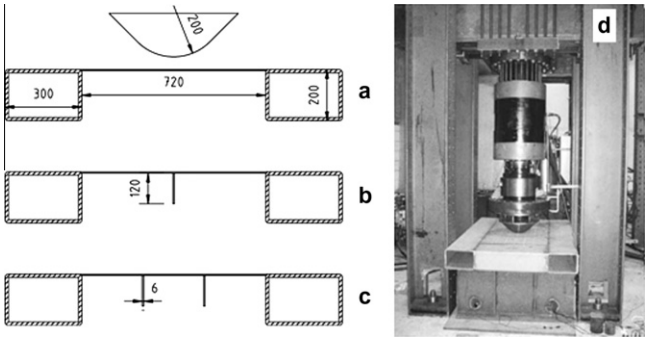

Fig. 2. Flat panel, stiffened plate configurations and experimental setup from (Alsos and Amdahl 2009).

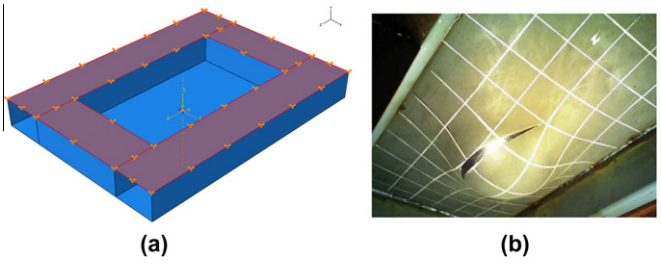

Fig. 3. (a) The boundary condition for the penetration of stiffened plate and flat panel. (b) The rupture of flat panel after indentation (Alsos and Amdahl 2009).

For this problem, the load was applied in terms of the lateral displacement of the indenter which is applied at a uniform rate of 0.6 m/s. When the speed of application of the load was slower than 2 m/s (Yamada et al., 2005) or 10 m/s (Ehlers, 2009) then no significant inertia effects are apparent. The penetration depth was set at 0.234 m and a friction coefficient of 0.3 was used.

The meshes chosen were 35, 25 and 15 mm. It was found that the best results for the FLD failure model, in term of a good correlation with the experimental data from (Alsos and Amdahl, 2009) were achieved with a 15 mm mesh size; see Fig. 4(a)–(c).

Although the results shown in Fig. 4(a) using a 35 mm element gave the best agreement when compared with the experimental values, overall the 15 mm element size gives the best correlation when considering all of the simulation results for the different structural models.

It can be observed in Fig. 4 that, for all mesh sizes, a good correlation is achieved up to where failure begins to occur. The prediction of failure/material rupture is most affected by the mesh size used to solve the problem, and hence mesh size appears to be directly related to the accurate prediction of failure.

It can also be observed in Fig. 4 that larger mesh sizes result in a delay in the onset of material failure, hence leading to an over-prediction of the maximum force. This is due to strain averaging occurring over a larger element area.

4.3. Simulation results

Results for the current FE model are presented in Figs. 5–7. These results are taken from the mesh convergence studies shown in Fig. 4 for the mesh size of 15 mm.

(a) Unstiffened flat panel

The force-displacement results for the penetration of the flat panel using different damage criteria are shown in Fig. 5(a) and (b). The current method using the FLD damage model coupled with the progressive failure model as previously discussed, predicted rupture at a vertical displacement of the penetrator of 180mm. This value is higher than those obtained using the BWH and most

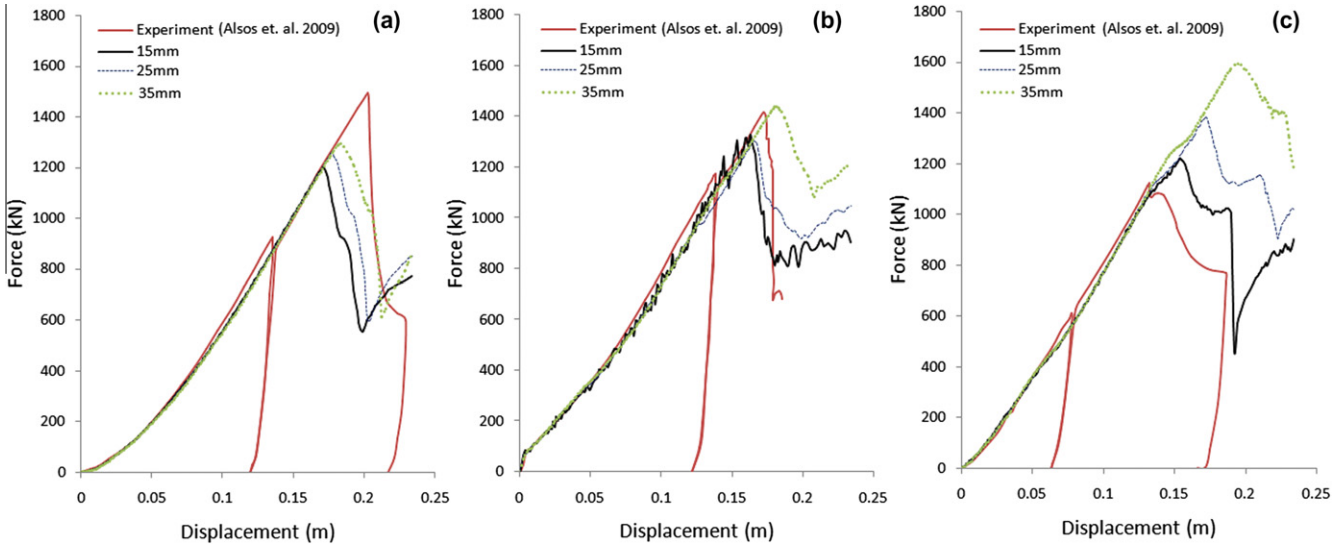

Fig. 4. Mesh convergence studies, (a) no stiffener, (b) single stiffener, and (c) two stiffeners.

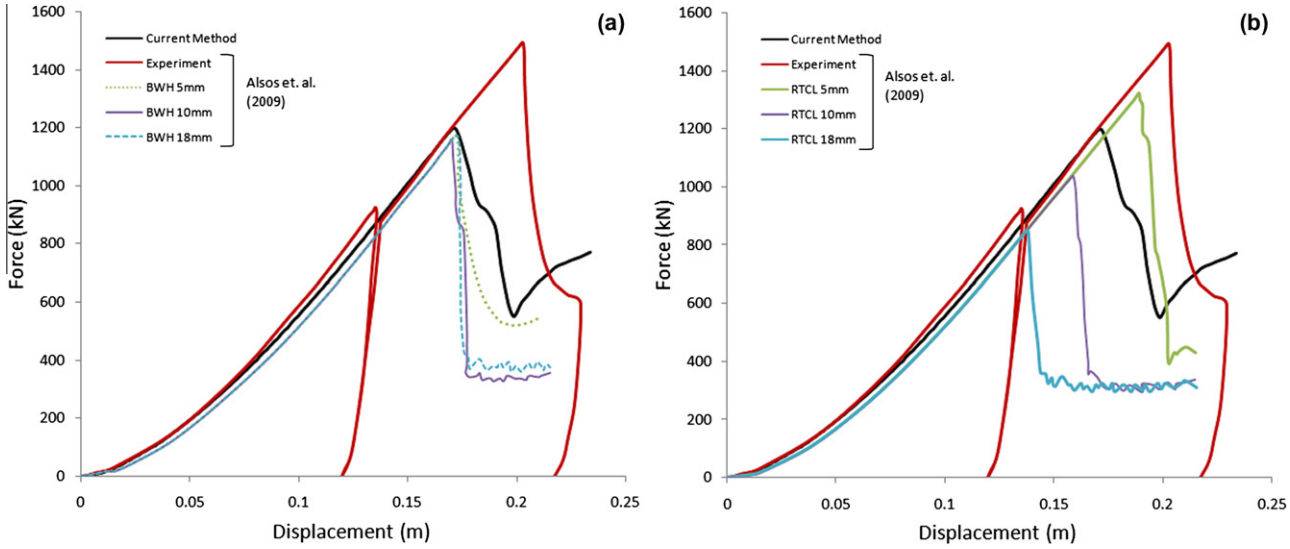

Fig. 5. Penetration of flat panel.

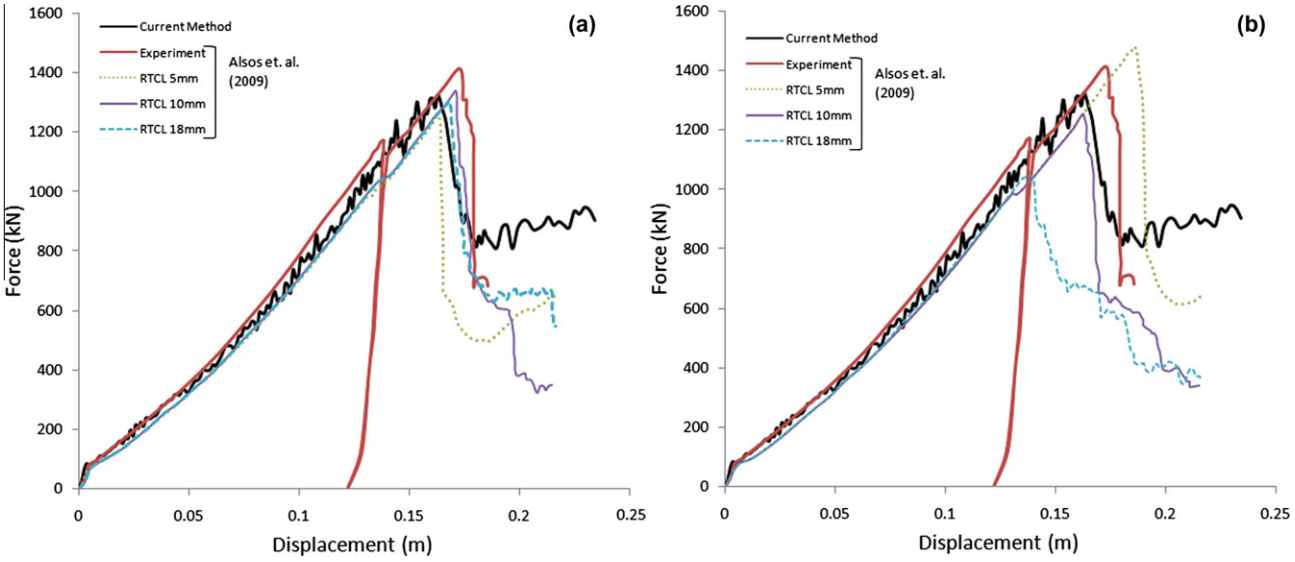

Fig. 6. Penetration on stiffener of single stiffened panel.

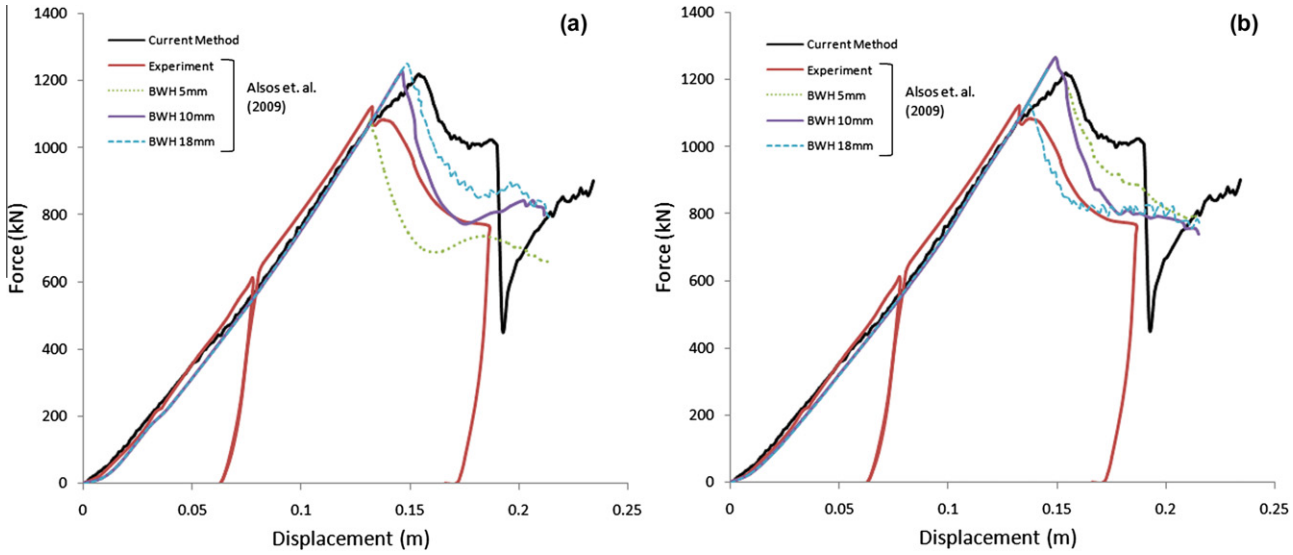

Fig. 7. Penetration of stiffened panel between two stiffeners.

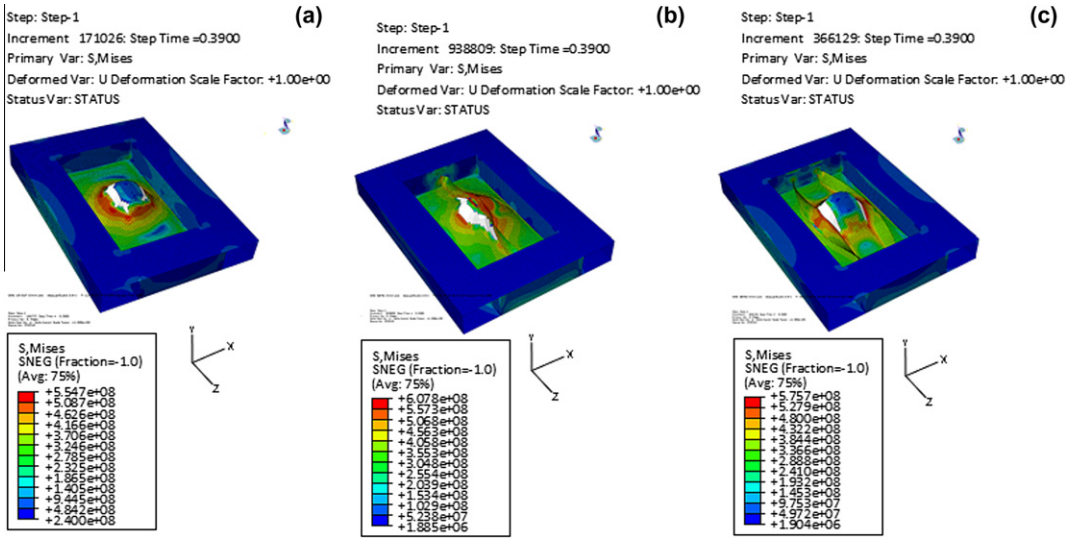

Fig. 8. The simulation of resistance of stiffened panels to penetration damage: (a) no stiffener, (b) single stiffener, (c) two stiffeners.

RTCL simulations. The BWH failure method predicted rupture at 175 mm, which is constant for most element mesh sizes; whereas the RTCL failure method predicted a scattered rupture at 120, 170 and 190 mm for mesh sizes of 18, 10 and 5 mm respectively. These predictions compare with the value of 200 mm obtained in the experiment. The numerical simulations appeared to give a good prediction of rupture initiation when compared with the experimental results. Fig. 8(a) shows the rupture damage predicted by the FE simulation which compares well with the experimental damage levels shown in Fig. 3(b) for this panel. This predicted fracture pattern was constant for all of the failure models i.e. FLD, RTCL and BWH.

(a) Single stiffened panel

The force-displacement results for the penetration of a single stiffened panel are shown in Fig. 6(a) and (b), where the current simulation predicts rupture at about the same level as the BWH and RTCL failure models. Depending on mesh size, rupture occurred at about 170 mm for the current FLD failure method using 15 mm mesh, and similar results were obtained for the BWH and RTCL failure models using 10 mm mesh. The simulation using the current FLD method gave good agreement with the experimental results leading to the conclusion that a 15 mm mesh size is likely to be most effective in this type of simulation using the progressive damage model described previously. Fig. 8(b) again shows the rupture damage pattern predicted by the FE solution.

(a) Panel with two Stiffeners

Force-displacement results are shown in Fig. 7(a) and (b). These show curves for the case of the penetration of a stiffened panel between two stiffeners, with graphs of penetrator force vs. displacement comparisons for both RTCL and BWH failure models. The RTCL and BWH models give variable results depending on the mesh size used in the simulations. The figures compare numerical predictions with experiment of results for both BWH and RTCL failure models using 5 and 18 mm element mesh sizes respectively.

The rupture predicted by the current FLD method using the 15 mm element size occurs at about 162 mm penetration, which compares well with both the BWH and RTCL for 18 and 5 mm element sizes respectively. In the current simulation, as shown in Fig. 8(c), the stiffeners seem to be tripping in the opposite direction to that observed in the experiment. This could be because the current simulations fail to consider the effects of welding and HAZ on stiffened panels, or it could be caused by slight offsets in the position where the impactor strikes the plating in the experiments.

4.4. Discussion of results

As is normal in FEA, the accuracy of the solution depends on the element type and mesh size. Given the limitations of the element formulations, finer meshes normally produce more realistic and accurate results. This is because a finer mesh usually gives a better representation of stress concentrations and also gives a better prediction of the strain in the element, hence providing a better prediction of the onset of failure.

In the current numerical simulations this was not always the case. For the RTCL damage criterion, the finer mesh produced less accurate results than the coarser mesh in almost all the simulations carried out when compared with experimental results. The current FLD failure criteria and the BWH criterion produce consistently similar results, and finer meshes give better correlation with experimental results as shown in Fig. 4(a)–(c).

The comparisons between numerical simulations and experimental results in this study are obviously valid for the mesh chosen and the material and rupture model used. Much more work needs to be carried out before any conclusion can be made about the applicability to other types of simulation.

It is easy for researchers to produce accurate results from numerical simulations when the answer we are trying to achieve is known. The mesh density can be varied as well as the modelling parameters until reliable results are achieved. Overall the current method demonstrates good convergence and a good correlation when compared to experimental results.

The attraction of the FLD approach to modelling material rupture is that it is very simple to construct the material failure diagram, which can account for both local necking and material rupture based on the simple tensile testing of materials.

5. Grounding damage experimental validation

Material failure modelling as discussed above is a crucial aspect of finite element analysis in producing reliable results for collision and grounding studies on steel ships. Therefore, further validation of the FE modelling technique was carried out using results from

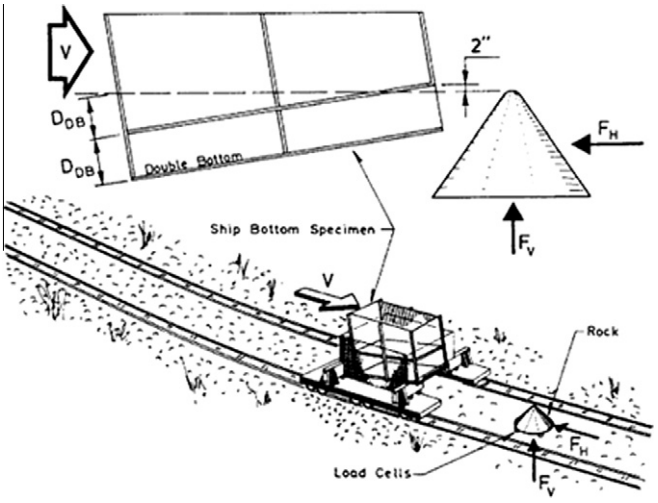

Fig. 9. Experiment configuration at the Naval Surface Warfare Center, USA (Rodd, 1996).

Table 2
The setup experiment properties by Naval Surface Warfare Center, USA, NSWC (Rodd, 1996).

Property	Value
Weight of model	223 tons
Model speed (V)	6.173 m/s
Rock tip radius	0.17 m
Rock apex angle	90°
Material	ASTM A569
Yield strength	283 MPa
Ultimate strength	345 MPa
Pitch angle (deg)	3.38

experimental studies carried out at the Naval Surface Warfare Center, USA (Rodd, 1996). The configuration of the test is shown in Fig. 9 and the properties involved are listed in Table 2.

The material employed for the finite element study is S235JR-EN10025 (B), where the strain hardening parameters used were 0.225 for FEA and 0.22 for the calculations carried at by (Simonsen, 1997). The FE results were compared with these of the experiment carried out by (Rodd, 1996) and the calculations by (Simonsen, 1997) which gave a very good correlation as shown in Fig. 10 and Fig. 11.

Fig. 11(a) shows the rupture of the structure from FEA using 15mm mesh and Fig. 11(b) show the actual damage to the structure during the experiment. The figures show significant levels of tearing of the inner bottom in both the FEA simulation and the experiment.

6. Grounding damage of double bottom structure

The use of FEA in crashworthiness analysis for double bottom structures has been considered by various authors (Amdahl and Kavlie, 1992; Naar et al., 2002; Wiśniewski and Kołakowski, 2003). Most of these studies use using both coarse and fine mesh densities to the demonstrate convergence of results. Recently, (Samuelides et al., 2007; Zilakos et al., 2009) have carried out the analysis of a similar structure, but using flat bar stiffeners instead of angle bar stiffeners on the outer and inner shell of the double bottom, as used in the current model. However, those simulations did not consider rupture failure in the model, but instead only looked at the extreme condition of the strength of the structure using fully plastic deformation prediction.

In the current simulation, both Von-Mises plastic deformation and rupture damage models were considered when investigating vertical grounding and longitudinal crushing along the compartment. In the vertical grounding simulation, all of the complexity of the structure and impact location that mentioned for the previous numerical simulations was taken into consideration. For longitudinal crushing the whole structure, including all inner and outer stiffeners, was considered due to the very long simulation times.

6.1. Structure geometry

A double bottom structure geometry was modelled as an idealised version of a real ship. Its particulars are as follows: LOA 265 m, LBP 256 m, beam 42.5 m, draught 15.65 m, GT (ITC 69)

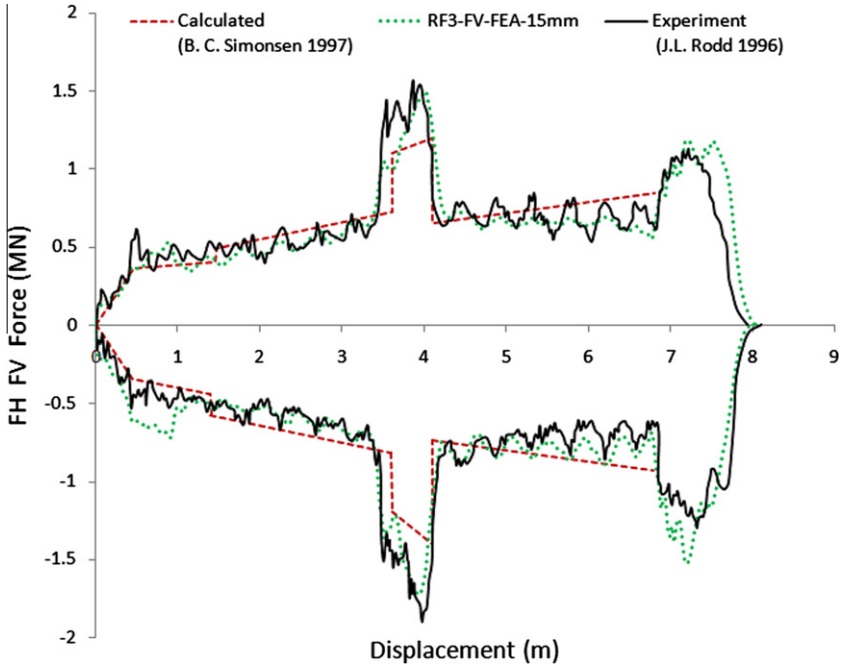

Fig. 10. Force displacement of NSWC1 model by Naval Surface Warfare Center, USA, (Rodd, 1996; Simonsen, 1997).

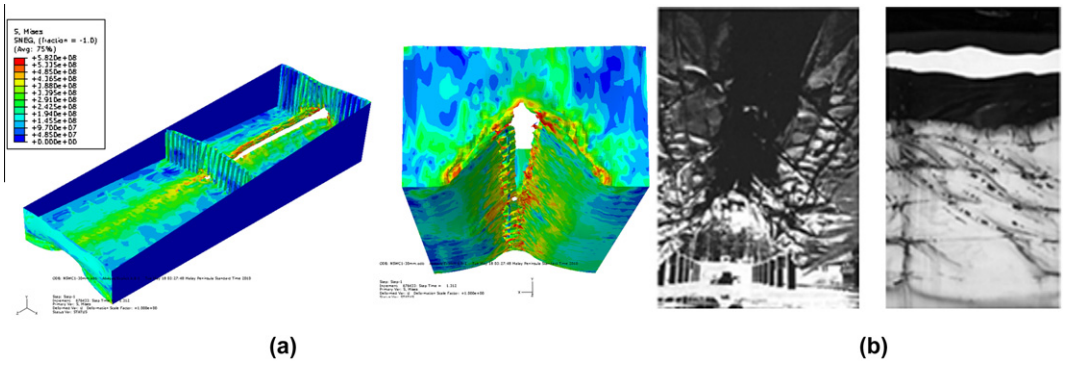

Fig. 11. (a) FEA simulation, (b) experimental results from the Naval Surface Warfare Center, USA (Rodd, 1996).

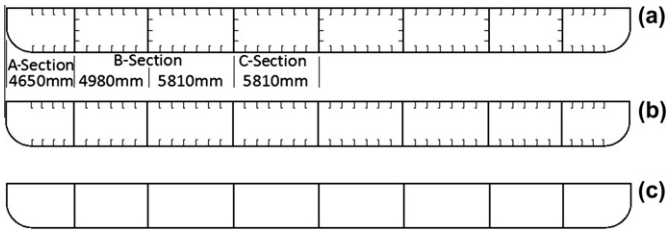

Fig. 12. Simplified models of double bottom.

Table 3
Thickness of the double bottom hull plating.

Types of structure member	Material	Thickness (mm)
Floor-1	C	15
Floor-2	C	15
Floor-3	C	15
Floor-4	C	16
Floor-5	C	15
Floor-6	C	15
Floor-7	C	15
A-Section stiffeners-16 of 400 × 14 mm	C	14
B-Section stiffeners-44 of 430 × 15 mm	C	15
A-Section stiffeners-16 of 400 × 16 mm	C	16
Floor stiffeners-21 of 300 × 14 mm	C	14
9 of Transverses	C	17
Inner plate	A	17
Outer plate	A	18

72.449T, and DWT 126.355T. The midship compartment was selected with a length of 32 m and a beam of 42.5 m. Nine transverse frames were included with a frame spacing of 4.0 m being assumed as constant throughout the compartment. The height between outer plating and inner plating was 2.97 m and spacing between vertical floors ranged from 4.65, 4.98, and 5.81 m, as shown in Fig. 12. All structural members were included in the numerical models, including outer plating, inner plating, longitudinal floors, transverses, outer plating stiffeners, inner plating stiffeners and longitudinal floor stiffeners.

Three alternative FE models were used to carry out the numerical simulations, as shown in Fig. 12; these were:

i Model A: All longitudinal stiffeners included in the model (ALLSI) see Fig. 12(a).
ii Model B: All longitudinal stiffeners included except stiffeners on longitudinal floors (SI) – see Fig. 12(b).
iii Model C: No longitudinal stiffeners included (ALLSNI); see Fig. 12(c)

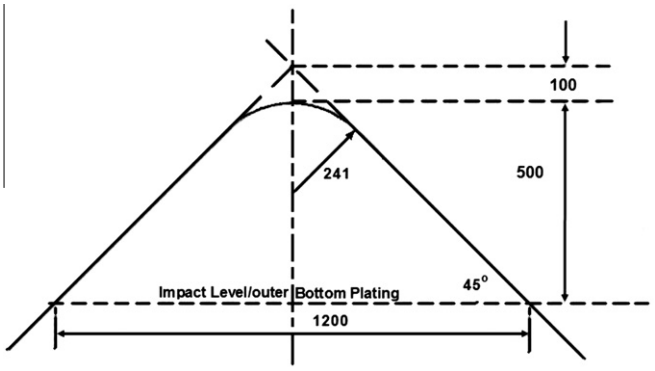

Fig. 13. Simplified rock with conical shape from (Zilakos et al., 2009).

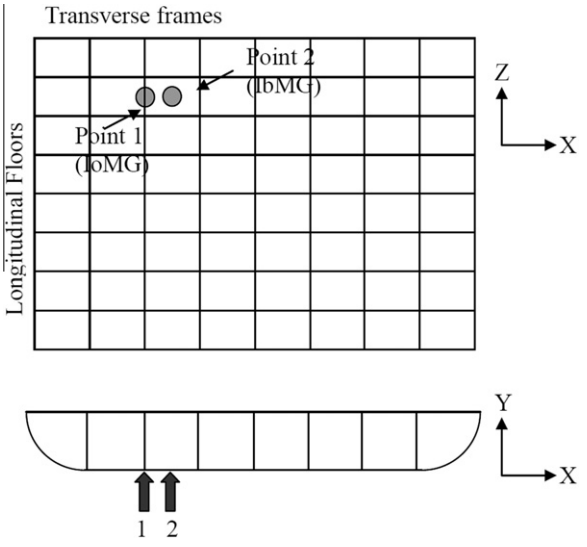

Fig. 14. Impact location on midship compartment (42.5 × 32 m.)

The details of the model arrangement and thickness of all plating and stiffeners are presented in Fig. 12(a)–(c) and Table 3. The rock geometry model was taken from (Zilakos et al., 2009) and is shown in Fig. 13.

6.2. Numerical approach

A mesh size of 15 mm was chosen based on the convergence study carried out in the previous simulation. The structure

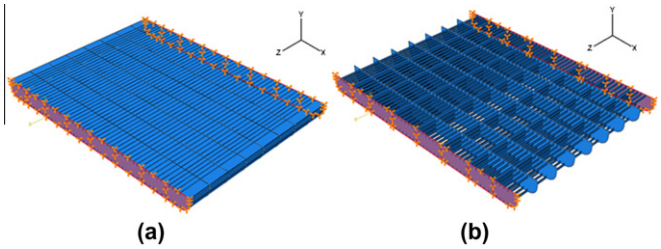

Fig. 15. Boundary condition set as ECANSTRE in red color (a) midship compartment (42.5 × 32 m) and (b) internal structure members. (For interpretation of the references to color in this figure legend, the reader is referred to the web version of this article.)

arrangement and location of crushing impact are both taken into consideration during the numerical simulations. The main impact locations considered were: impact on main transverse frame (IoMG), and impact between the main transverse frames (IbMG) as shown in Fig. 14.

The friction coefficient was set at 0.3 for all of the simulations, which is applicable for most cases of mild steel surface contact. The analyses utilised a structured quadrilateral dominated mesh for fine as well as coarse mesh regions, and unstructured mesh for the transition region.

The speed of the vessel was taken as being that of a typical ship at a service speed of 10 m/s or 19.4 knots, and it was assumed to be constant during the grounding simulation. This speed has been used by other researchers such as (Samuelides et al., 2007; Zilakos et al., 2009) in similar studies.

There are two different phases of impactor movement during these analyses. Phase 1 involve vertical movement or penetration of the double bottom to a depth of 0.5 m in the Y-direction. This is followed by phase 2 which is horizontal movement, travelling

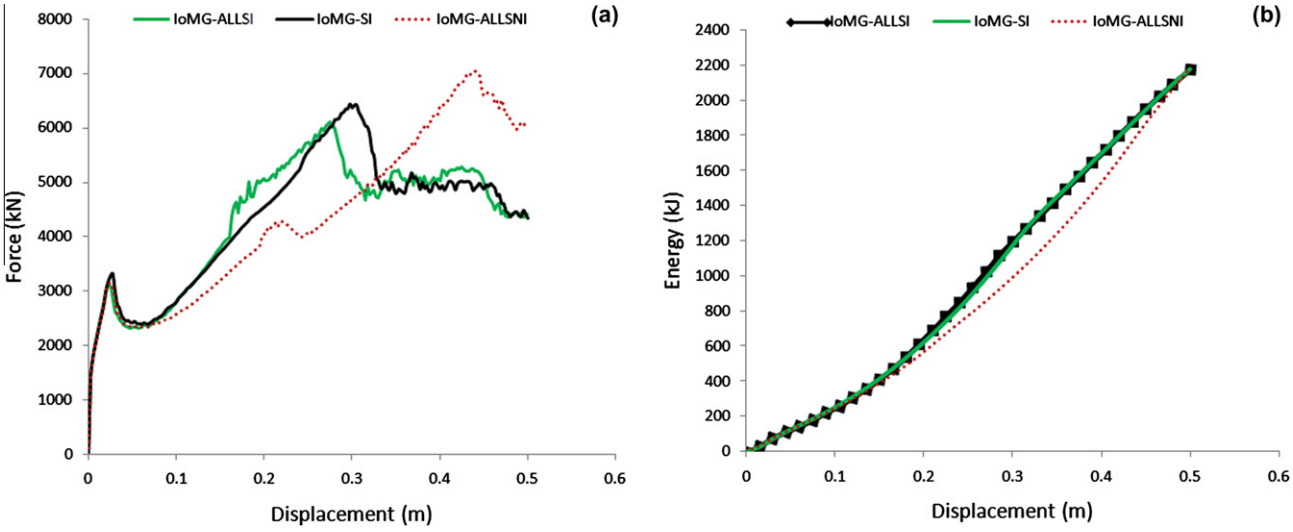

Fig. 16. Impact on main floor (a) force – penetrator displacement and (b) energy – penetrator displacement

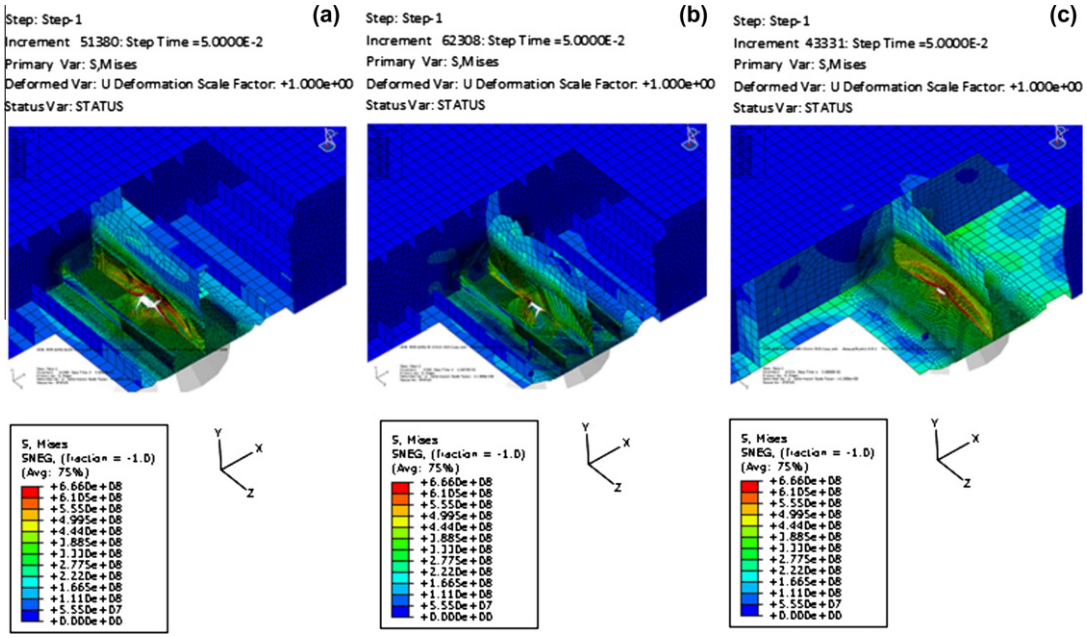

Fig. 17. Phase 1. The simulation of vertical grounding displacement for impact on main floor on models a, b and c.

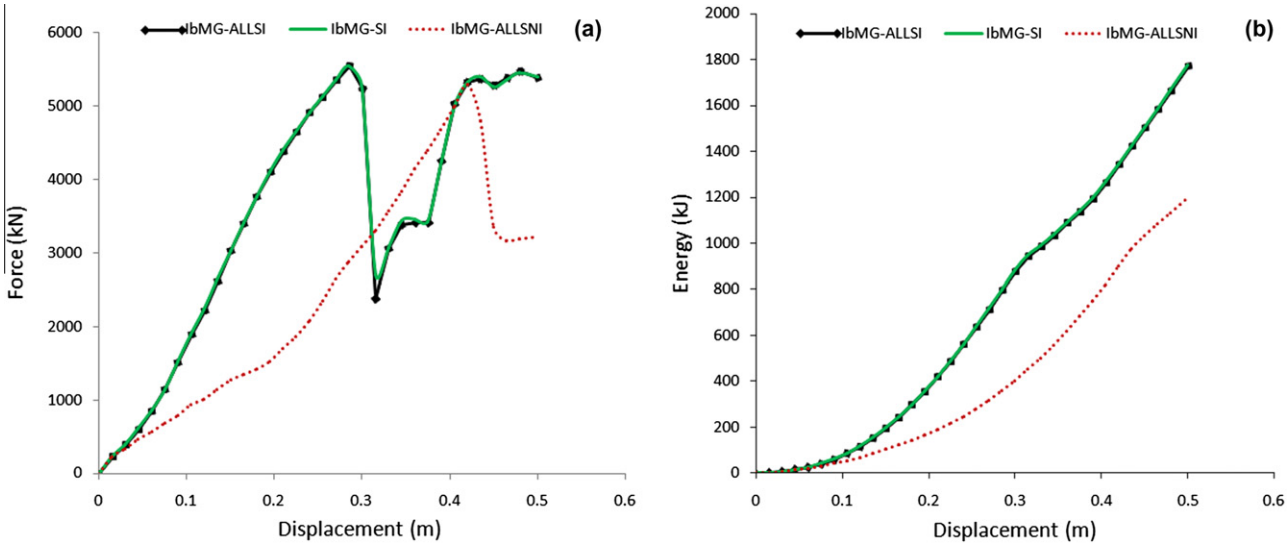

Fig. 18. Impact between main floors (a) force – penetrator displacement, and (b) energy – penetrator displacement

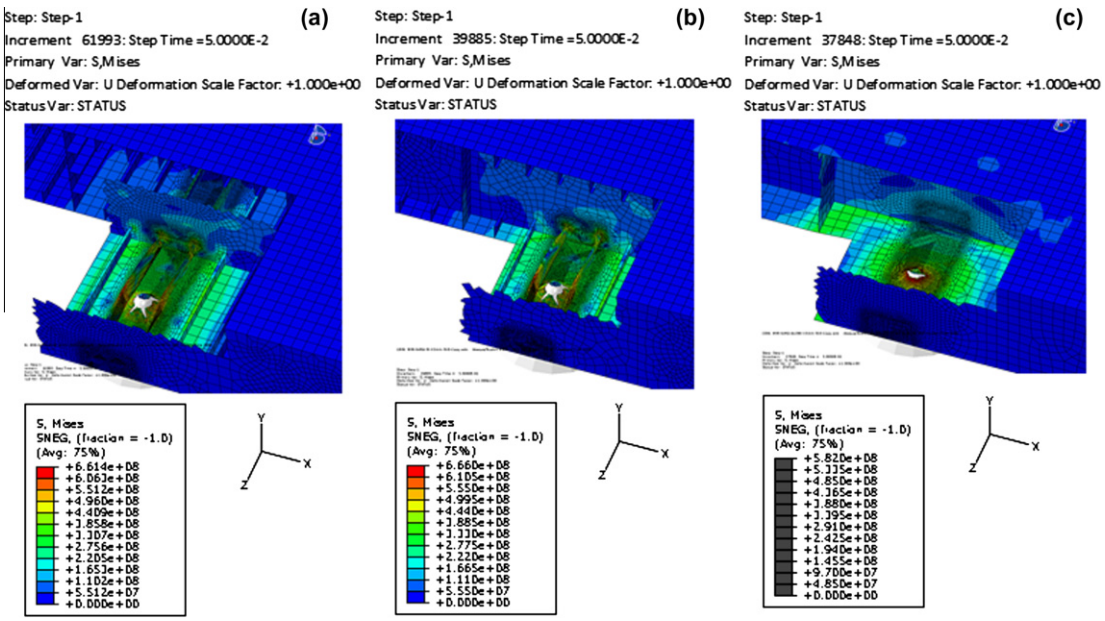

Fig. 19. Phase 1. The simulation of vertical grounding displacement for model a, b, and c impact between main floors.

about 13 m in the Z direction (−ve). Phase 1 simulated the early stage of rupture of the double bottom which happens during grounding. Phase 2 simulated the significant damage and rupture which occurs in the structure as the ship's momentum moves it forward.

All the analyses were carried out using the strain based failure criterion described previously in the material failure model. The boundary conditions were set as ESCANSTRE (fully fixed) for both ends of the transverse frames (see Fig. 15), due to the presence of transverse watertight bulkheads at these positions. The analysis was run without considering the effect of strain rate. For the cases considered here, where the grounding speed is only 10 m/s, this is a reasonable assumption to make.

The analyses were carried out using two types of desktop computers which use single processor Intel Core i7, 12 GB RAM, and dual Intel Xeon E5540, 24GB RAM systems. Most of the analyses generated file sizes ranging from 25–40 GB, with running time between 300–360 h, and using a range of elements between 154,229 and 254,790 for the complete simulation; this includes vertical penetration and horizontal crushing during grounding. The dual Intel Xeon processor was faster during simulations compared to the single processor when the same analysis was run on both machines.

6.3. Simulation results

In this section, the progressive failure of the double bottom is discussed, considering both the effect of damage due to the plastic deformation of the double bottom and also the evolution of damage including material rupture. In phase 1, the extreme grounding simulation of the vertical penetration of the double bottom was carried out by looking at force displacement and energy displacement relationships for all models. In phase 2, the main focus was to look at fully plastic deformation and material

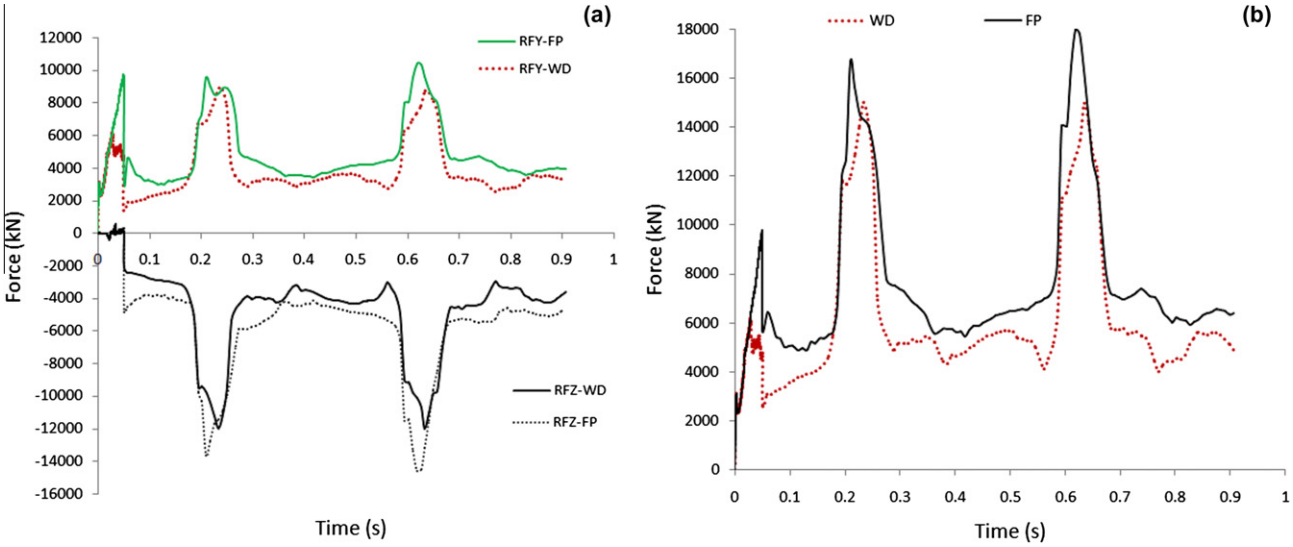

Fig. 20. Impact on main floor (a) the grounding force in Y (RFY) and Z (RFZ) directions, and (b) the resultant force.

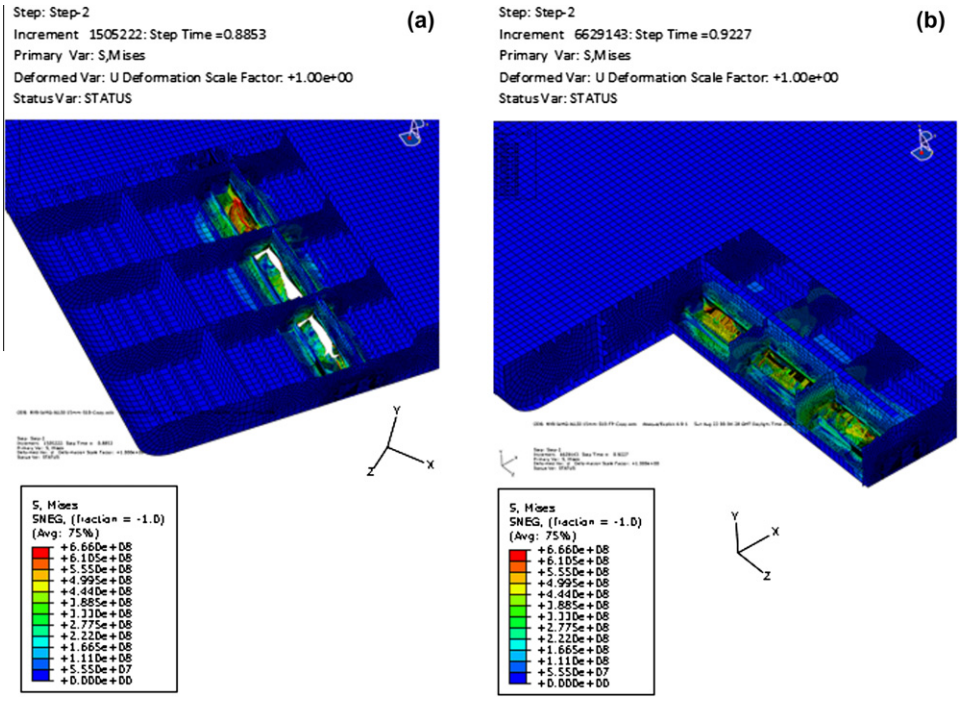

Fig. 21. Impact on main floor (a) with damage (b) without damage.

degradation against time due to grounding, only using model A (ALLSI).

Phase 1: Vertical grounding

The results for impact on the main floor are shown in Fig. 16. Fig. 16(a) shows that the structure for model C was capable of resisting a higher force and displacement before rupture, followed by model B and then model A. Material rupture takes place at 0.30, 0.32 and 0.45 m of penetration for models A, B and C respectively. The figure also indicates the significant effect of modelling stiffeners and their contribution to failure during impact.

This shows that the stiffness of the structure plays an important role in the onset of rupture. A more rigid structure will give a lower crashworthiness capability compared to a more flexible structure from the point of view of hull rupture. Looking at Fig. 16(b), it can be seen that the energy absorbed by the structure is of a similar magnitude in all three models. The model without any longitudinal stiffeners, Model C, deviates slightly from models A and B, but ends up at the same point of 0.5 m of displacement and 2.2 MJ crushing energy.

The responses of the models to vertical grounding on the main transverse floor are shown in Fig. 17(a)–(c). These clearly show that damage started to occur on the bottom plating during grounding, mainly due to the large local deformation and strain being generated by the penetrator.

The forces generated during phase 1 grounding between the main transverse floors are shown in Fig. 18(a) for models A and B and are almost identical, with rupture occurring at 0.31 m vertical displacement and 5.6 MN maximum force. This indicates that stiff-

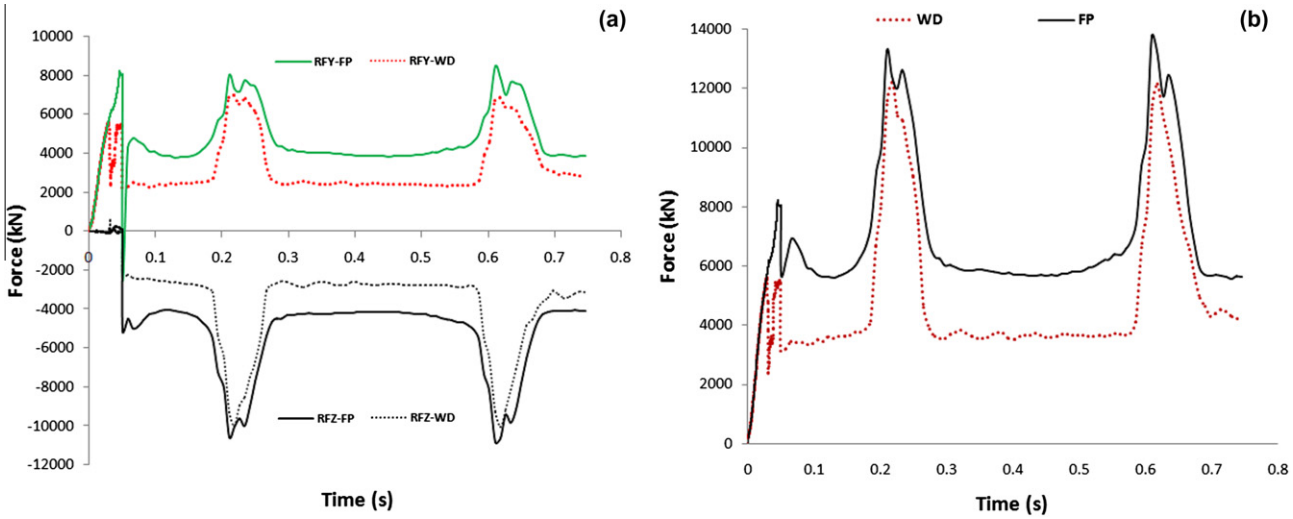

Fig. 22. Impact between main floors the grounding force in Y (RFY) and Z (RFZ) direction, and (b) the resultant force.

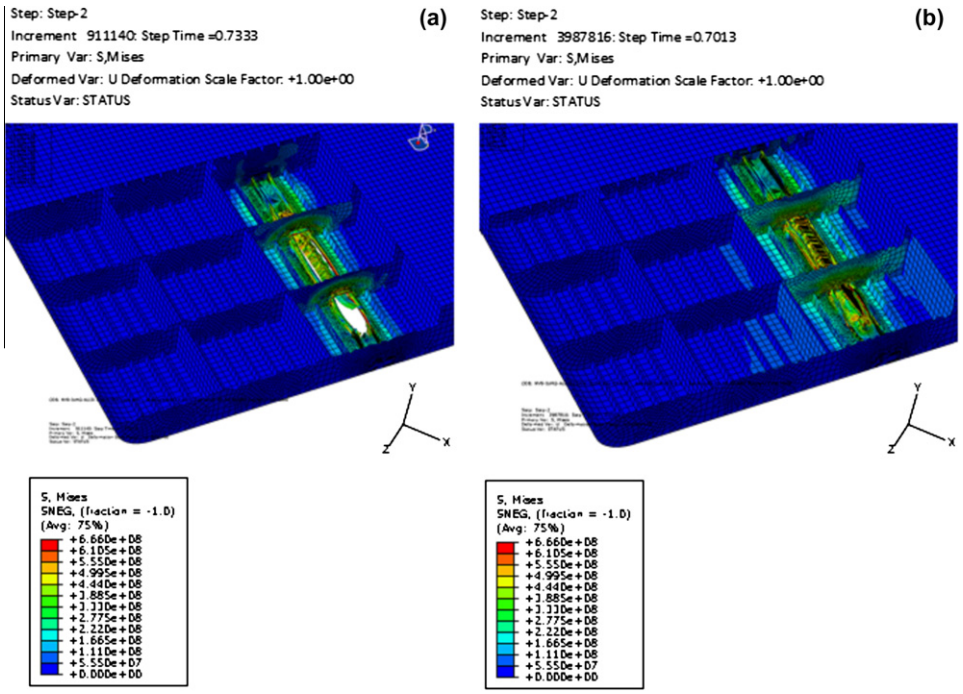

Fig. 23. Impact between main floors, (a) dith damage (b) without damage.

eners on the main longitudinal floor do not appear to contribute significantly to the strength of the structure during this phase of grounding. But when all of the stiffeners in the structure are removed, the penetrator is able to cause greater deformation before rupture is initiated, which occurs at 0.44 m vertical displacement. Fig. 18(b) shows a similar pattern where the level of energy for models A and B are the same giving 1.78 MJ at a vertical displacement of 0.5 m. The energy for model C is lower than those for models A and B, giving 1.20 MJ at the same displacement.

The behaviour of the structures during the simulations are shown in Fig. 19(a)–(c), where models A and B again behave in the same manner and show similar rupture propagation tendencies. For model C the rupture pattern displays similar patterns to that shown in the simplified experiment carried out by (Alsos and Amdahl, 2009).

The depth of penetration and subsequent grounding damage was chosen to be consistent with the results of (Samuelides et al., 2007; Zilakos et al., 2009), since this is part of the same study.

Phase 2: Horizontal Crushing during grounding

The next stage in the simulation was to investigate the horizontal crushing of the double bottom, after rupture, due to the forward momentum of the ship. Fig. 20(a) and (b) show the grounding force on the double bottom for the midship compartment. Fig. 20 also shows the fully plastic (FP) force which would be obtained if the simulation had been carried out without modelling material failure (WD), and this demonstrates that higher forces are produced for this simulation than when material failure modelling is included in the simulation. In Fig. 20(a) we can see that the maximum grounding forces during the crushing of the transverse floors are RFY = 10.4 MN and RFZ = −14.6 MN, for fully plastic, and

RFY = 8.74 MN and RFZ = −12 MN for when material failure properties are included.

When we look at the resultant crushing force on the double bottom, as shown in Fig. 20(b), the grounding force when neglecting material failure is always higher than when we include material rupture. The difference between them can be estimated to be about 15–50%, where the peak forces for phase 1 are 9.69 MN and 17.96 MN and for phase 2, 6.18 MN and 15.01 MN for FP and WD failure models respectively. The performance of the structure in both conditions can be seen clearly in Fig. 21(a) and (b). In Fig. 21(a), the tearing of the plate during grounding is due to high stress concentrations which can be observed to occur at the joint between the floor and the bottom plate. In Fig. 21(b), the elements display only stretching, without showing any tearing or rupture.

Fig. 22 shows the response of the structure when the grounding occurs between the main transverse floors followed by longitudinal tearing of the structure. The same behaviour as before is shown in Fig. 22(a) and (b), where a larger force is generated without modelling the rupture of the structure than when rupture is modelled.

The difference between FP and WD failure modelling produces differences in the range of 11–40% for the force generated. In Fig. 22(a), RFY and RFZ forces peak at 8.47 MN and −10.84 MN respectively for FP, and 6.86 MN and −10 MN respectively for WD. The resultant maximum force for phases 1 and 2, as shown in Fig. 22(b), are 8.2, 13.76 and 5.54, 12.22 MN for FP and WD respectively.

The failure mechanisms in the structure are clearly shown in Fig. 23(a) and (b). Fig. 23(a) shows the failure of the structure during grounding with the plate tearing close to the longitudinal stiffeners. Fig. 23(b) shows the bottom plate elements stretching in the middle of the span between longitudinal bottom plate stiffeners without any rupture.

6.4. Discussion

In this analysis it has been demonstrated that a more rigid structure is less crashworthy than a more flexible structure when considering hull rupture. This phenomenon is clearly demonstrated in Phase 1 of the simulation, where the penetration of the indenter shows higher displacements before the initiation of rupture in model C than in models A and B. This simulation also showed that not including material rupture (FP) always produces higher failure loads than when rupture is modelled (WD), where simulations demonstrate higher results by about 30–50% for Phase 1 and 11–35% for Phase 2.

The results in Phase 2 also show a good correlation with the finding of (Zilakos et al., 2009) where the maximum force for RFY-FP and RFZ-FP during crushing of the transverse floors demonstrates an almost constant level of force throughout the simulation irrespective of the number of transverse floors. The results obtained for RFY-FP and RFZ-FP simulations are also higher than (Zilakos et al., 2009), which is reasonable due to the higher plastic material properties those of used, (Zilakos et al., 2009) used 245 MPa as the material yield stress whereas the current model used properties as defined in Table 1.

The analysis also found that the estimated onset of material rupture in Phase 1 is very sensitive to the material failure model adopted. The differences between fully plastic and material failure models in Phase 1 clearly show significant differences. It has also been demonstrated that the effect of grounding is very much localised in all simulations. This can be seen in the localisation of high stress contours, which only occur in the area close to the impact location.

7. Conclusion

The purpose of this study was to use the finite element method to investigate grounding damage to ship structures. This was achieved by looking at available experimental data and calculations using FE analysis, and then applying the grounding methodology developed to the study damage to the structure of ship bottoms.

This is a very complex process and the calculations are dependent on mesh size, types of loading, crushing location, boundary conditions and the software that is being used in the analysis. Although many studies have been conducted on this topic, their results exists considerable variability. Therefore, a significant amount of discussion and explanation with regard to the accuracy and reliability of results is still required.

Overall, the results obtained from the FEA simulations of penetration are acceptable when compared to these of the actual experiments (Alsos and Amdahl, 2009; Alsos et al., 2009) and produced very good agreement when compared to the experimental results of grounding damage (Yamada et al., 2005).

The grounding simulation also showed good correlation with previously published results (Samuelides et al., 2007; Zilakos et al., 2009) in term of penetration force.

This demonstrates that FEA is an appropriate tool which can be used to investigate the local and global behaviour of a ship's structure during grounding, providing that good models for predicting material rupture are employed which should include appropriate scaling laws to take account of mesh size sensitivity effect.

Numerical simulations are cheaper to run than experimental studies, but there is still a significant requirement to carry out of good quality experimental studies. Results from such experiments are necessary for validating numerical simulation models in predicting structural responses during collision and grounding. The comparisons of experiments and numerical modelling studies will help establish suitable numerical models for carrying out future assessments of collision and grounding scenarios.

8. Future work

Present study has concluded that, for the prediction of material failure, an element mesh size of 15 mm was suitable for the simulations carried out. However, accurate force-displacement response can be simulated using much coarser mesh sizes.

Therefore more work is required to investigate the use of scaling laws in conjunction with FLD failure criteria. This will enable larger element sizes to be used while still retaining the accurate prediction of material rupture.

This will help to reduce the time taken for computational costs of simulation, thus enabling larger structural models to be analysed. This approach looks very promising and further results will be presented in a future publication.

Acknowledgements

This work has been conducted within the context of the Network of Excellence on Marine Structures (MARSTRUCT) which was partially funded by the European Union through the Growth Programme under contract TNE3-CT-2003-506141.

References

ABAQUS, ABAQUS Analysis User's Manual, Version 6.8, Dassault Systèmes Simulia Corporation.

Alsos, H.S., Amdahl, J., 2007. On the resistance of tanker bottom structures during stranding. Marine Structures 20 (4), 218–237.

Alsos, H.S., Amdahl, J., 2009. On the resistance to penetration of stiffened plates, Part I – Experiments. International Journal of Impact Engineering 36 (6), 799–807.

Alsos, H.S., Amdahl, J., et al., 2009. On the resistance to penetration of stiffened plates, Part II: Numerical analysis. International Journal of Impact Engineering 36 (7), 875–887.

Alsos, H.S., Hopperstad, O.S., et al., 2008. Analytical and numerical analysis of sheet metal instability using a stress based criterion. International Journal of Solids and Structures 45 (7–8), 2042–2055.

Amdahl, J., Kavlie, D. 1992. Experimental and numerical simulation of double hull stranding, in: DNV-MIT Workshop on Mechanics of Ship Collision and Grounding.

Ehlers, S., 2009. A procedure to optimize ship side structures for crashworthiness. Proceedings of the Institution of Mechanical Engineers Part M: Journal of Engineering for the Maritime Environment 224 (1), 1–11.

Hill, R., 1991. A theoretical perspective on in-plane forming of sheet metal. Journal of the Mechanics and Physics of Solids 39 (2), 295–307.

Hutchinson, J.W, Neale, K.W. 1978. Sheet necking-III. Strain-rate effects, in: Mechanics of Sheet Metal Forming, 269–285.

Jie, M., Cheng, C.H., et al., 2009. Forming limit diagrams of strain-rate-dependent sheet metals. International Journal of Mechanical Sciences 51 (4), 269–275.

Keeler, S.P., Backofen, W.A., 1963. Plastic instability and fracture in sheets stretched over rigid punches. Transactions ASM 56 (1), 25–48.

Kitamura, O., 2002. FEM approach to the simulation of collision and grounding damage. Marine Structures 15 (4–5), 403–428.

Lehmann, E., Peschmann, J., 2002. Energy absorption by the steel structure of ships in the event of collisions. Marine Structures 15 (4–5), 429–441.

Naar, H., Kujala, P., et al., 2002. Comparison of the crashworthiness of various bottom and side structures. Marine Structures 15 (4–5), 443–460.

Rodd, J.L. 1996. Observations on conventional and advanced double hull grounding experiments, in: Int. Conf. on Designs and Methodologies for Collision and Grounding Protection of Ships, 13.11–13.13.

Samuelides, M.S., Voudouris, G., et al. 2007. Simulation of the behaviour of double bottoms subjected to grounding actions, in: Proceedings of the fourth International Conference on Collision and Grounding of Ships (ICCGS).

Simonsen, B.C. 1997. Mechanic of ship grounding. Ph.D Dissertation, Department of Naval Architecture and Offshore Engineering, Technical University of Denmark, Denmark.

Wiśniewski, K., Kołakowski, P., 2003. The effect of selected parameters on ship collision results by dynamic FE simulations. Finite Elements in Analysis and Design 39 (10), 985–1006.

Yamada, Y., Endo, H., et al. 2005. Numerical study on the effect of buffer bow structure in ship–ship collision, in: Proceedings of the International Offshore and Polar Engineering Conference, Seoul.

Yu, H.L., Jeong, D.Y., 2010. Application of a stress triaxiality dependent fracture criterion in the finite element analysis of unnotched Charpy specimens. Theoretical and Applied Fracture Mechanics 54 (1), 54–62.

Zhang, A., Suzuki, K. 2005. Numerical simulation the bottom structure grounding test by LS-DYNA, in: Fifth European LS-DYNA Users Conference.

Zilakos, I., Toulios, M., et al. 2009. Simulation of the response of double bottoms under grounding actions using finite elements. in: Proceedings of MARSTRUCT 2009, Second International Conference on Marine Structures-Analysis and Design of Marine Structures, Lisbon.